

# *In situ* SEM Study of Lithium Intercalation in individual V<sub>2</sub>O<sub>5</sub> Nanowires

*Evgheni Strelcov*<sup>†1,2</sup>, *Joshua Cothren*<sup>2</sup>, *Donovan Leonard*<sup>3</sup>, *Albina Y. Borisevich*<sup>3</sup>, and *Andrei Kolmakov*<sup>4</sup>

<sup>1</sup>Center for Nanophase Materials Sciences, Oak Ridge National Laboratory, Oak Ridge,  
Tennessee 37831

<sup>2</sup>Department of Physics, Southern Illinois University at Carbondale, Carbondale, Illinois 62901

<sup>3</sup>Materials Science and Technology Division, Oak Ridge National Laboratory, Oak Ridge,  
Tennessee 37831

<sup>4</sup>Center for Nanoscale Science and Technology, National Institute of Standards and Technology,  
Gaithersburg, Maryland 20899

**KEYWORDS:** V<sub>2</sub>O<sub>5</sub> nanowires, lithiation, *in situ* SEM, ionic liquid

---

<sup>†</sup> Corresponding author: [strelcove@ornl.gov](mailto:strelcove@ornl.gov)

## **ABSTRACT:**

Progress in rational engineering of Li-ion batteries requires better understanding of the electrochemical processes and accompanying transformations in the electrode materials on multiple length scales. In spite of recent progress in utilizing transmission electron microscopy (TEM) to analyze these materials, *in situ* scanning electron microscopy (SEM) was mostly overlooked as a powerful tool that allows probing these phenomena on the nano and mesoscale. Here we report on *in situ* SEM study of lithiation in a V<sub>2</sub>O<sub>5</sub>-based single-nanobelt battery with ionic liquid electrolyte. Coupled with cycled voltammetry measurements, *in situ* SEM revealed the peculiarities of subsurface intercalation, formation of solid-electrolyte interface (SEI) and electromigration of liquid. We observed that single-crystalline vanadia nanobelts do not undergo amorphization or fracture during electrochemical cycling, but rather transform topochemically with only a slight shape distortion. The SEI layer seems to have significant influence on the lithium ion diffusion and overall capacity of the single-nanobelt battery.

## **INTRODUCTION:**

The increasing demand for smaller, lighter, cheaper, and longer-lasting power sources for portable electronics, aircrafts and vehicles impels intensive research of the lithium ion batteries.<sup>1</sup> <sup>2</sup> Implementation of the modern paradigm of rational battery engineering, including design of smart electrode materials, is impossible without in-depth understanding of the chemical and physical processes in galvanic cells at the microscopic, nanoscopic, and eventually, molecular levels. Reaction mechanisms, cathode expansion, formation of cracks and solid electrolyte interface layer, electrolyte decomposition etc., are being extensively studied with a variety of *ex* and *in situ* microscopic, spectroscopic and electrochemical techniques: optical<sup>3</sup>, electron<sup>4-10</sup> and

scanning probe<sup>11-13</sup> microscopy, NMR,<sup>14, 15</sup> x-ray photoelectron spectroscopy,<sup>16</sup> x-ray<sup>17</sup> and neutron<sup>18</sup> diffraction, etc.. *In situ* transmission electron microscopy of single-nanowire batteries is the most recent advancement of the battery characterization, allowing real-time monitoring of the electrochemical processes at the nano and atomic scales.<sup>4, 19, 20</sup> However, most of the cathode materials chosen for studies so far – SnO<sub>2</sub>,<sup>4, 21, 22</sup> ZnO,<sup>23</sup> Si,<sup>5, 6, 24</sup> Ge,<sup>20</sup> RuO<sub>2</sub><sup>25</sup> – do not manifest topochemical transformations during lithiation, but rather lose their crystalline structure irreversibly as a result of reduction, pulverization or amorphization processes. For instance, a single crystal SnO<sub>2</sub> nanowire upon lithiation first irreversibly transforms into a conglomerate of clumped nanoparticles of Li<sub>2</sub>O and metallic tin:  $SnO_2 + 4Li^+ + 4e^- \rightarrow Sn + 2Li_2O$ ; and only after that can the tin nanoparticles be reversibly cycled:  $Sn + xLi^+ + xe^- \rightleftharpoons Li_xSn$ . Lithium oxide, thus, remains idle, forming a bulky and unnecessary ballast. These processes lead to a significant expansion and loss of electrical and mechanical integrity of the nanostructured cathodes, and therefore, shorten the battery lifetime and capacity. Vanadium pentoxide, on the contrary, is not reduced to metal during lithiation, but rather, as a classical intercalation material, forms a continuous range of lithium bronzes Li<sub>x</sub>V<sub>2</sub>O<sub>5</sub> with  $0 < x < 3$ .<sup>26-28</sup> Hence, its well-known  $\epsilon$ ,  $\delta$ ,  $\gamma$  and  $\omega$ -phases<sup>27</sup> can be reversibly cycled (Fig. 1a) from low to high lithium content with only a moderate expansion of the lattice<sup>26, 27, 29</sup> (Fig. 1b-c). Orthorhombic V<sub>2</sub>O<sub>5</sub> has a layered structure consisting of graphene-like 2D sheets joined by weak van der Waals interaction (Fig. 1c). Intercalation of lithium in the interlayer space leads to progressive puckering of the layers and partial reduction of vanadium oxidation state from +5 to +4, which lowers the electrochemical potential of the formed bronze. When the number of lithium ions per V<sub>2</sub>O<sub>5</sub> unit cell exceeds 1, the lattice irreversibly transforms into the  $\gamma$ -structure (also orthorhombic, P<sub>nma</sub>), which, in turn, is irreversibly converted into the tetragonal  $\omega$ -phase when lithium content exceeds 2 atoms per

$V_2O_5$  unit cell. Despite the irreversibility of the structural transformations, the material does not lose its integrity and all of the phases can be reversibly lithiated/delithiated the following ranges:  $\epsilon$  in the  $0 < x < 0.5$ ,  $\delta$  in the  $0.5 < x < 1$ ,  $\gamma$  in the  $1 < x < 2$ ,  $\omega$  in the  $2 < x < 3$ .

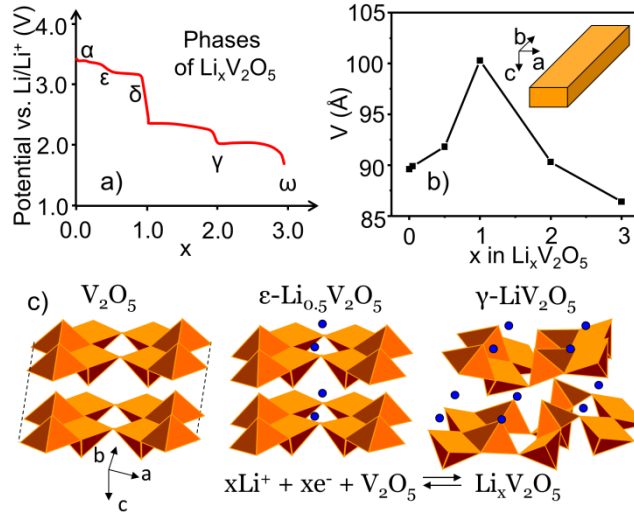


**Figure 1.**  $Li_xV_2O_5$  bronzes: a) Potential-stoichiometry dependence of a  $Li/V_2O_5$  cell showing 5 bronze phases (adapted from Ref. [27]); b) Volume of the unit cell per 1  $V_2O_5$  structure as a function of bronze stoichiometry; inset shows direction of the  $V_2O_5$  unit cell axes relative to nanobelt; c) Structures of pure  $V_2O_5$  and two bronze phases showing puckering of the tetrahedral layers as a consequence of lithium intercalation.

Most of the prior *in situ* research has been focused on TEM (HRTEM) characterization of the model cathodic (anodic) materials. Despite the great advantage in lateral and spectroscopic quality of the data, these experiments remain to be a challenging task. Here, we would like to focus on *in situ* SEM,<sup>30-32</sup> which has the advantage of prompt mesoscopic morphological and chemical *in situ* characterization of energy materials. In particular, we report on an *in situ* SEM study of lithium intercalation in  $V_2O_5$  employing a single-nanobelt battery.

## RESULTS AND DISCUSSION:

*In situ* SEM lithiation measurements were conducted using custom made experimental setup shown schematically in Figure 2a. A palladium wire sharpened into a needle served both as a growth substrate for V<sub>2</sub>O<sub>5</sub> nanobelts (NBs) and the working electrode. The direct growth of vanadia whiskers at the Pd wire apex excluded the need for commonly used transfer of the grown NBs to the electrode and gluing them to it. The working electrode was mounted on a micromanipulator allowing for precise control of the NBs position. The counter/reference electrode was formed by a flattened gold wire with mechanically embedded LiCoO<sub>2</sub> powder as a Li source. A drop of 8% g/g solution of bis(trifluoromethane)sulfonamide of lithium in ionic liquid (1-butyl-1-methylpyrrolidinium bis(trifluoromethylsulfonyl)imide) was drop casted on the Au/LiCoO<sub>2</sub> electrode and spread over its sides providing the liquid electrolyte environment. The whole assembly was placed inside the vacuum chamber of the SEM and connected to the electrical circuitry. Using a micromanipulator different individual NBs could be submerged into the liquid in a controlled way. Figure 2b shows a backscattered electrons (BSE) SEM micrograph of the assembled single-whisker battery (micron-thick whiskers were used to record current with sufficiently high signal-to-noise ratio). By cycling the voltage of the working electrode from +0.5 V to -2.2 V and back and recording current from the counter/reference electrode, lithium intercalation into the whisker/NB can be monitored, with sequential formation of all known bronze phases (see cyclic voltammogram of Fig. 2c). Since the formation of the  $\omega$ -phase is irreversible (*i.e.* it cannot be converted to other phases), deintercalation is seen as two very broad anodic peaks. Having identified the peak voltages of all phases in the extended voltammogram by comparing it to the literature data, we further focused on a narrower voltage window, where reversible formation of the  $\delta$  and  $\epsilon$  phases takes place (see Fig. 2d

voltammogram with two cathodic and anodic peaks). Since our SEM setup was a two-electrode configuration, and Au/LiCoO<sub>2</sub> pseudo reference electrode was used, the positions of the peak voltages of individual phases were subject to linear shifts, when switching to a new electrode or NB, as can be seen by comparing voltammograms of Fig. 2c and 2d. Despite this, the intensity and positions of peaks relative to each other remained fairly constant. Another noticeable shortcoming of the two-electrode system was the appreciable polarization of the electrodes seen in the steeply decaying current at the onset of measurements (around +0.5 V in the voltammogram). However, the latter did not influence the formation of the  $\delta$  and  $\epsilon$  phases or their reversibility, as can be seen from comparing the two curves of Figure 2d. The black curve of the first cycle has a polarization tail; the red one of the second cycle lacks it, but their overall shapes are almost the same.

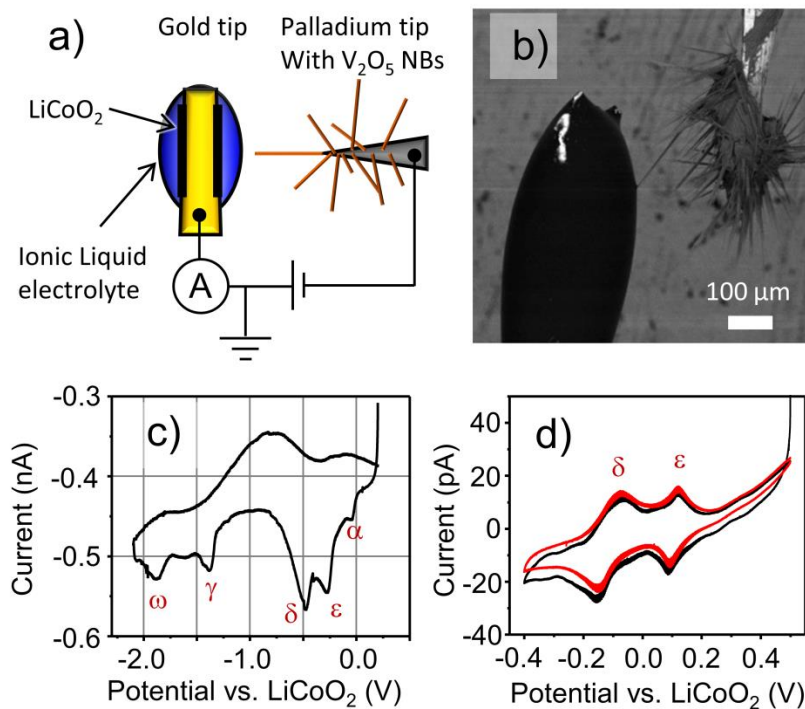


**Figure 2.** Single- $V_2O_5$  nanobelt battery: a) Schematic of the experimental setup; b) Backscattered electron detector SEM micrograph of the assembled battery with one  $V_2O_5$  whisker submerged in electrolyte; c)-d) Cyclic voltammograms of two single-whisker battery devices highlighting sequential formation of bronze phases; potential was swept from positive to negative polarity and back; panel d) shows two sequential bias sweeps, red being the second one; sweep rate is  $85 \mu\text{V/s}$ .

The phenomena observed *in situ* during the single-NB battery discharging can be classified into three categories: (i). NB expansion due to intercalation, (ii). NB shape distortion, (iii). Electrocapillary motion of the liquid electrolyte. Although the total lattice volume per one  $V_2O_5$  unit initially increases and then decreases as the amount of intercalated lithium increases from 0 to 3 per unit cell (Fig. 1b), this change is unevenly distributed between the unit cell axes, and, accordingly, the NB dimensions. The NB thickness should expand the most, as the puckering of layers occurs, and the  $\delta$  phase is formed. Upon further increase in lithium content the bronze

structure changes irreversibly to a more close-packed one ( $\gamma$ -phase), which leads to a decrease in thickness. The NB thickness expansion happens upon application of negative potential to the NB submerged in electrolyte as shown in Figure 3. The image recorded 620 s after application of -2.2 V to the NB (Fig. 3b) shows the formed expansion front propagating away from the liquid along the NB length. At 758 s (Fig. 3c) the front shifts more to the left, but at 1037 s (Fig. 3d) it is overtaken by the advancing electrolyte front that electromigrates in the same direction. Both fronts are clearly seen at the initial stages of intercalation, when the expansion front moves faster than the liquid front. Later, however, the expansion front propagation slows down and the spreading of liquid over the NB surface smears the image making the expansion front barely visible. and the presence of liquid leads to formation of SEI seen as a bulge on the NB surface. In an attempt to reverse this process, a positive potential of +0.5 V was applied to the NB at 1584s, after which the liquid front slowly recedes (Fig. 3f), leaving behind the exposed SEI bulge. Thus, of all the electrochemical processes involved only Li intercalation and electromigration of electrolyte can be manipulated reversibly.

Another aspect of the electrochemical changes the NB undergoes is its distortion: a shape change different from expansion. Figure 4 shows a NB that was submerged into electrolyte 49  $\mu\text{m}$  deep. Two subsequent cyclic voltammograms were recorded (Fig. 3g) and the NB was pulled out of liquid to reveal its newly-coiled tip. Note, that this bending is present after the reversible intercalation/deintercalation cycles are complete, and thus must be due to uneven expansion of the BN sides and the remnant stress. The voltammograms allow for quantification of the amount of intercalated/deintercalated lithium, and volume of the NB that was affected by this process. The latter is given by:

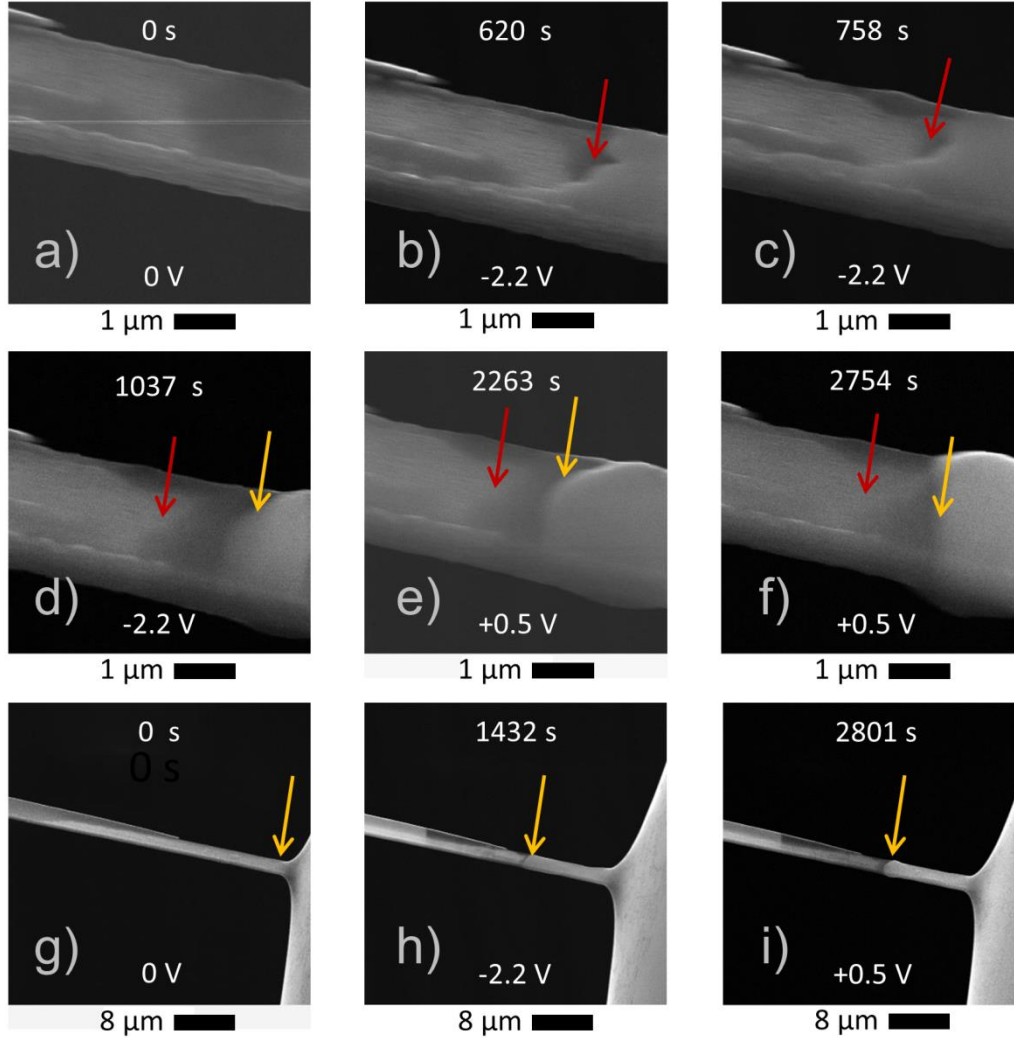


**Figure 3.** *In situ* morphological changes: a)-f) Expansion of the NB thickness during discharging process at indicated biases; liquid droplet is situated to the right of the scanning frame; expansion front (red arrow) propagates to the left and is taken over by liquid (yellow arrow) spreading over the NB due to electrocapillary action; the expansion front in d) is masked by the spread liquid; positive potential (+0.5 V) was applied to the NB at 1584 s, after which time liquid began to slowly withdraw exposing modified surface of the NB; g)-i) Low magnification images of same NB at different potentials showing easily-identifiable advancing and receding liquid fronts (yellow arrows).

$$V = \frac{QM_{V_2O_5}}{eN_A\rho V_2O_5} \quad (1)$$

where  $Q$  is the integral charge of intercalation/deintercalation,  $M$  and  $\rho$  are the molar mass and density of  $V_2O_5$ ,  $e$  is the elementary charge, and  $N_A$  is the Avogadro number. Since the terminal formed phase was  $\delta$ - $LiV_2O_5$ , participation of one lithium ion in electrochemical processes corresponds to one  $V_2O_5$  unit involved. The integral charge was calculated by integrating the corresponding current segments shown in Figure 4g over time (which was recorded during cycling, but is not shown here). The integral charge for intercalation ( $Q_{C\varepsilon} + Q_{C\delta} = (1.13 \pm 0.06) \cdot 10^{-9}$  C) is almost equal to that for deintercalation ( $Q_{A\varepsilon} + Q_{A\delta} = (1.17 \pm 0.05) \cdot 10^{-9}$  C), which confirms that the process was completely reversed and no lithium remained in the distorted NB. Thus, according to Eq. 1, the volume of intercalation was about  $0.7 \mu\text{m}^3$ . The NB was *ca.* 280  $\mu\text{m}$  long, 450 nm wide and 400 nm thick close to its tip, with its foremost 49  $\mu\text{m}$  submerged into the electrolyte. Hence the volume of the submerged part of the NB was an order of magnitude larger than the volume of intercalation, which means that intercalation must have affected only the surface regions of the NB, leaving its core bulk intact. Similar near intercalation was previously observed for chemical lithiation of large  $V_2O_5$  NB.<sup>33</sup> The time passed since the onset of the  $\varepsilon$ -phase formation to the onset of the  $\delta$  anodic peak was 3 hr 19 min ( $t_1$  to  $t_2$  in Fig. 4g). Knowing the elapsed time and diffusion coefficient of lithium ions, an estimate of the diffusion depth can be made.  $Li^+$  diffusivity in thin  $V_2O_5$  films grown by thermal evaporation in a vacuum and annealed at 500 °C (in Ar) was reported<sup>34</sup> to increase from  $0.3 \cdot 10^{-12}$   $\text{cm}^2/\text{s}$  for  $V_2O_5$  to  $100 \cdot 10^{-12}$   $\text{cm}^2/\text{s}$  for  $\delta$ - $LiV_2O_5$ . Films annealed at 200 °C showed<sup>34</sup> a different behavior – a linear decrease of diffusivity during intercalation, so that  $D_{Li}$  in the  $\delta$ -phase is  $0.03 \cdot 10^{-12}$   $\text{cm}^2/\text{s}$ . The NBs studied in the current work were annealed in a vacuum at *ca.* 500 °C. The smallest value of the diffusivity should be the limiting factor determining the possible

diffusion depth. In the provided time the smallest values of  $D_{Li}$  yield a diffusion distance of ca. 590 nm ( $D_{Li}$  for  $V_2O_5$ ) and 190 nm ( $D_{Li}$  for  $\delta$ - $LiV_2O_5$  annealed at 500 °C).

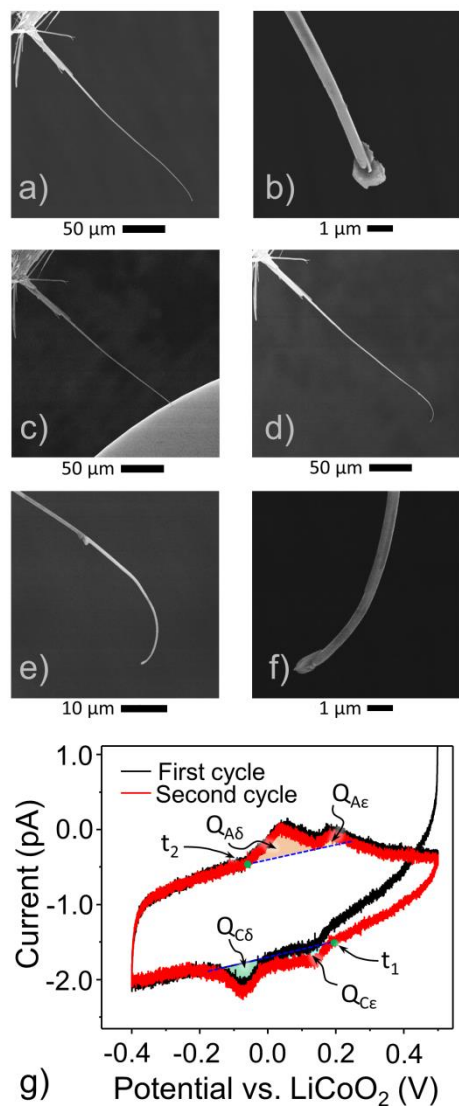


**Figure 4.** *In situ* morphological changes - bending: a)-b) Initial shape of a  $V_2O_5$  NW (overview and zoomed-in image of the NW tip); c) NW immersed into liquid electrolyte; d) NW pulled out of electrolyte after discharging (overview); e)-f) final NW distortion shown at two different magnifications (compare the NW tip shape before and after – panels b and f); Cyclic voltammogram of same NW showing formation of the  $\epsilon$  and  $\delta$  bronze phases; potential was swept from positive to negative polarity and back;

sweep rate is 85  $\mu\text{V/s}$ ; The charge of intercalation/deintercalation was calculated for each peak separately by integrating the highlighter regions over time.

These values are comparable or higher than the average effective radius of the NB, which implies that the diffusion of  $\text{Li}^+$  in the NB was slower than in the films reported in [34]. Two reasons can explain this difference. Firstly,  $D_{\text{Li}}$  obviously varies depending on the diffusion path, with the slowest diffusion happening along the c-axis, perpendicular to the  $\text{V}_2\text{O}_5$  layered structure. Any measurement performed on polycrystalline films necessarily detects the fastest diffusion coefficient along the dimension, which may not be easily accessible in the single crystal NB. The facet perpendicular to the b-axis of the NB has the smallest area, and the one perpendicular to the c-axis – the largest. Secondly, accumulation of SEI layer, observed in our experiments, may hamper intercalation resulting in an apparently decreased  $\text{Li}^+$  diffusion coefficient.

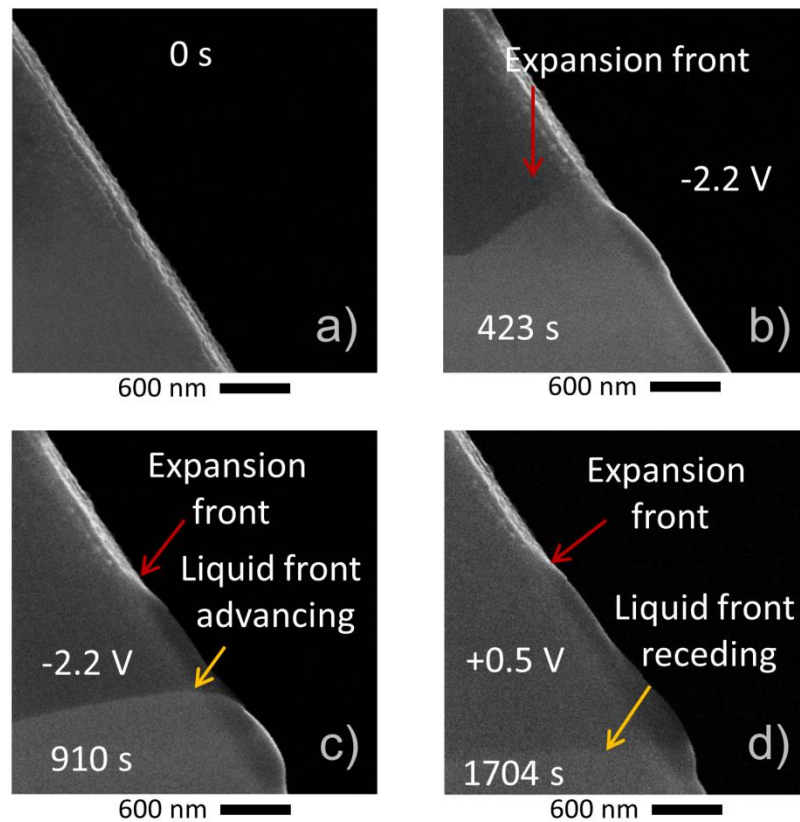


**Figure 5.** *In situ* morphological changes: a) Initial view of the whisker edge; b) View of the thickness expansion front moving upward as the battery discharges; liquid front is outside of the image frame; c) Liquid front advances, too, which changes the image contrast and makes the expansion front barely visible; d) After application of positive bias (at 1133 s), the liquid front recedes, leaving behind laterally expanded surface and SEI; expansion front remains at approximately same distance as before.

Formation of the SEI layer is detailed in Figure 5 that highlights the edge of a NB anode. Application of negative bias to the NB onsets propagation of the thickness expansion front (Fig 5b) as well as motion of electrolyte that lags behind (Fig. 5c). The advancing liquid front brings with it an SEI layer that deposits on the NB surface and is mostly concentrated at the liquid-vacuum interface. As the electrolyte recedes in response to the application of positive potential, the SEI becomes exposed (Fig. 5d). Its formation is irreversible and it accumulates on the surface over time, leading to a decrease in capacitance of the nanobattery during repetitive cycling.

In summary, we demonstrate the usefulness of the *in situ* SEM studies of charge-discharge cycles in model single crystal  $V_2O_5$  nanobelt battery with  $LiCoO_2$  anode in a vacuum-compatible ionic liquid electrolyte. Cyclic voltammetry and potentiometric curves were correlated with the SEM observed processes such as electromigration, formation of SEI and NB expansion, revealing that lithiation occurs near the surface and is presumably significantly affected by the SEI. It is shown that  $V_2O_5$  NBs can reversibly intercalate lithium without structural integrity failure or cracks formation, and underwent only minimal shape distortions.

## **MATERIALS AND METHODS:**

$V_2O_5$  NBs were grown by a catalyst-free thermal evaporation method from  $V_2O_5$  powder precursor. NBs grew on Pd needles mounted on the Pt microheater of an optical cell, as

described in [35]. The temperatures of the source and Pd needles were controlled independently. The whiskers synthesis was monitored *in situ* through an optical microscope and stopped at the desired length of NBs. Upon growth termination, the NBs were annealed in the same cell for  $\approx 1$  min at  $\approx 500$  °C (until their bright-orange color changed to dull-brown indicating partial oxygen loss) to increase their electronic conductivity. Bis(trifluoromethane)sulfonamide of lithium (LiTfSI) was dissolved in 1-butyl-1-methylpyrrolidinium bis(trifluoromethylsulfonyl)imide to form an 8% g/g solution. The Au/LiCoO<sub>2</sub> counter/reference electrode was chosen due to its higher stability in air as compared to metal lithium, since transfer of the nanobattery from the glove box to the SEM imaging chamber necessitated brief air exposure. The employed ionic liquid is hydrophobic, which served as additional protection of the electrolyte from the water vapor present in the air. Electrolyte preparation was performed in an argon-filled glove box. The potential waveform generation and current recording was done using a DAQ card controlled through a custom-written code. A current amplifier was used to detect current. Uncertainty in the integral charge of intercalation was calculated from the signal-to-noise ration of the current measurements.

#### **ACKNOWLEDGEMENTS:**

Research supported by the Materials Science and Engineering Division of the U.S. Department of Energy and through a user project supported by ORNL's Center for Nanophase Materials Sciences (CNMS), which is sponsored by the Scientific User Facilities Division, Office of Basic Energy Sciences, U.S. Department of Energy. SIUC part of the research was supported through NSF ECCS-0925837 grant. Authors are thankful to Dr. Yigal Lilah for his help in LabView programming. ES and AK would like to thank Dr. Sergei V. Kailinin for fruitful discussions of the present work.

## REFERENCES

- (1) Tarascon, J. M.; Armand, M. *Nature* **2001**, *414*, 359.
- (2) Choi, N. S.; Chen, Z. H.; Freunberger, S. A.; Ji, X. L.; Sun, Y. K.; Amine, K.; Yushin, G.; Nazar, L. F.; Cho, J.; Bruce, P. G. *Angewandte Chemie-International Edition* **2012**, *51*, 9994.
- (3) Harris, S. J.; Timmons, A.; Baker, D. R.; Monroe, C. *Chem. Phys. Lett.* **2010**, *485*, 265.
- (4) Huang, J. Y.; Zhong, L.; Wang, C. M.; Sullivan, J. P.; Xu, W.; Zhang, L. Q.; Mao, S. X.; Hudak, N. S.; Liu, X. H.; Subramanian, A.; Fan, H.; Qi, L.; Kushima, A.; Li, J. *Science* **2010**, *330*, 1515.
- (5) Liu, X. H.; Wang, J. W.; Huang, S.; Fan, F.; Huang, X.; Liu, Y.; Krylyuk, S.; Yoo, J.; Dayeh, S. A.; Davydov, A. V.; Mao, S. X.; Picraux, S. T.; Zhang, S.; Li, J.; Zhu, T.; Huang, J. Y. *Nat Nano* **2012**, *7*, 749.
- (6) McDowell, M. T.; Lee, S. W.; Harris, J. T.; Korgel, B. A.; Wang, C.; Nix, W. D.; Cui, Y. *Nano Letters* **2013**, *13*, 758.
- (7) Ruzmetov, D.; Oleshko, V. P.; Haney, P. M.; Lezec, H. J.; Karki, K.; Baloch, K. H.; Agrawal, A. K.; Davydov, A. V.; Krylyuk, S.; Liu, Y.; Huang, J.; Tanase, M.; Cumings, J.; Talin, A. A. *Nano Letters* **2011**, *12*, 505.
- (8) Lee, S.; Oshima, Y.; Hosono, E.; Zhou, H.; Kim, K.; Chang, H. M.; Kanno, R.; Takayanagi, K. *The Journal of Physical Chemistry C* **2013**, *117*, 24236.
- (9) Su, Q.; Du, G.; Zhang, J.; Zhong, Y.; Xu, B.; Yang, Y.; Neupane, S.; Li, W. *ACS Nano* **2014**, *8*, 3620.
- (10) Liu, Y.; Fan, F.; Wang, J.; Liu, Y.; Chen, H.; Jungjohann, K. L.; Xu, Y.; Zhu, Y.; Bigio, D.; Zhu, T.; Wang, C. *Nano Letters* **2014**, *14*, 3445.
- (11) Balke, N.; Jesse, S.; Morozovska, A. N.; Eliseev, E.; Chung, D. W.; Kim, Y.; Adamczyk, L.; Garcia, R. E.; Dudley, N.; Kalinin, S. V. *Nat Nano* **2010**, *5*, 749.
- (12) Kalinin, S. V.; Balke, N. *Adv. Mat.* **2010**, *22*, E193.
- (13) Światowska-Mrowiecka, J.; Maurice, V.; Klein, L.; Marcus, P. *Electrochemistry Communications* **2007**, *9*, 2448.
- (14) Grey, C. P.; Dupré, N. *Chem. Rev.* **2004**, *104*, 4493.
- (15) Holland, G. P.; Buttry, D. A.; Yarger, J. L. *Chemistry of Materials* **2002**, *14*, 3875.
- (16) Światowska-Mrowiecka, J.; Maurice, V.; Zanna, S.; Klein, L.; Marcus, P. *Electrochimica Acta* **2007**, *52*, 5644.

- (17) Meulenkamp, E. A.; van Klinken, W.; Schlatmann, A. R. *Solid State Ionics* **1999**, *126*, 235.
- (18) Kim, H.; Lee, S.; Park, Y. U.; Kim, H.; Kim, J.; Jeon, S.; Kang, K. *Chemistry of Materials* **2011**, *23*, 3930.
- (19) Wang, C. M.; Xu, W.; Liu, J.; Choi, D. W.; Arey, B.; Saraf, L. V.; Zhang, J. G.; Yang, Z. G.; Thevuthasan, S.; Baer, D. R.; Salmon, N. *Journal of Materials Research* **2010**, *25*, 1541.
- (20) Liu, X. H.; Liu, Y.; Kushima, A.; Zhang, S.; Zhu, T.; Li, J.; Huang, J. Y. *Advanced Energy Materials* **2012**, *2*, 722.
- (21) Wang, C.-M.; Xu, W.; Liu, J.; Zhang, J.-G.; Saraf, L. V.; Arey, B. W.; Choi, D.; Yang, Z.-G.; Xiao, J.; Thevuthasan, S.; Baer, D. R. *Nano Letters* **2011**, *11*, 1874.
- (22) Nie, A.; Gan, L.-Y.; Cheng, Y.; Asayesh-Ardakani, H.; Li, Q.; Dong, C.; Tao, R.; Mashayek, F.; Wang, H.-T.; Schwingenschlögl, U.; Klie, R. F.; Yassar, R. S. *ACS Nano* **2013**, *7*, 6203.
- (23) Kushima, A.; Liu, X. H.; Zhu, G.; Wang, Z. L.; Huang, J. Y.; Li, J. *Nano Letters* **2011**, *11*, 4535.
- (24) Liu, X. H.; Zheng, H.; Zhong, L.; Huang, S.; Karki, K.; Zhang, L. Q.; Liu, Y.; Kushima, A.; Liang, W. T.; Wang, J. W.; Cho, J.-H.; Epstein, E.; Dayeh, S. A.; Picraux, S. T.; Zhu, T.; Li, J.; Sullivan, J. P.; Cumings, J.; Wang, C.; Mao, S. X.; Ye, Z. Z.; Zhang, S.; Huang, J. Y. *Nano Letters* **2011**, *11*, 3312.
- (25) Gregorczyk, K. E.; Liu, Y.; Sullivan, J. P.; Rubloff, G. W. *ACS Nano* **2013**, *7*, 6354.
- (26) Cocciantelli, J. M.; Doumerc, J. P.; Pouchard, M.; Broussely, M.; Labat, J. *Journal of Power Sources* **1991**, *34*, 103.
- (27) Delmas, C.; Cognac-Auradou, H.; Cocciantelli, J. M.; Ménétrier, M.; Doumerc, J. P. *Solid State Ionics* **1994**, *69*, 257.
- (28) Baddour-Hadjean, R.; Marzouk, A.; Pereira-Ramos, J. P. *Journal of Raman Spectroscopy* **2012**, *43*, 153.
- (29) Rocquefelte, X.; Boucher, F.; Gressier, P.; Ouvrard, G. *Chemistry of Materials* **2003**, *15*, 1812.
- (30) Kolmakova, N.; Kolmakov, A. *The Journal of Physical Chemistry C* **2010**, *114*, 17233.
- (31) Krueger, M.; Berg, S.; Stone, D. A.; Strelcov, E.; Dikin, D. A.; Kim, J.; Cote, L. J.; Huang, J.; Kolmakov, A. *ACS Nano* **2011**, *5*, 10047.
- (32) Jensen, E.; Købler, C.; Jensen, P. S.; Mølhav, K. *Ultramicroscopy* **2013**, *129*, 63.
- (33) Chan, C. K.; Peng, H.; Twisten, R. D.; Jarausch, K.; Zhang, X. F.; Cui, Y. *Nano Letters* **2007**, *7*, 490.
- (34) Scarminio, J.; Catarini, P. R.; Urbano, A.; Gelamo, R. V.; Rouxinol, F. P.; de Moraes, M. A. B. *J. Braz. Chem. Soc.* **2008**, *19*, 788.
- (35) Strelcov, E.; Davydov, A. V.; Lanke, U.; Watts, C.; Kolmakov, A. *ACS Nano* **2011**, *5*, 3373.

Supporting Information:

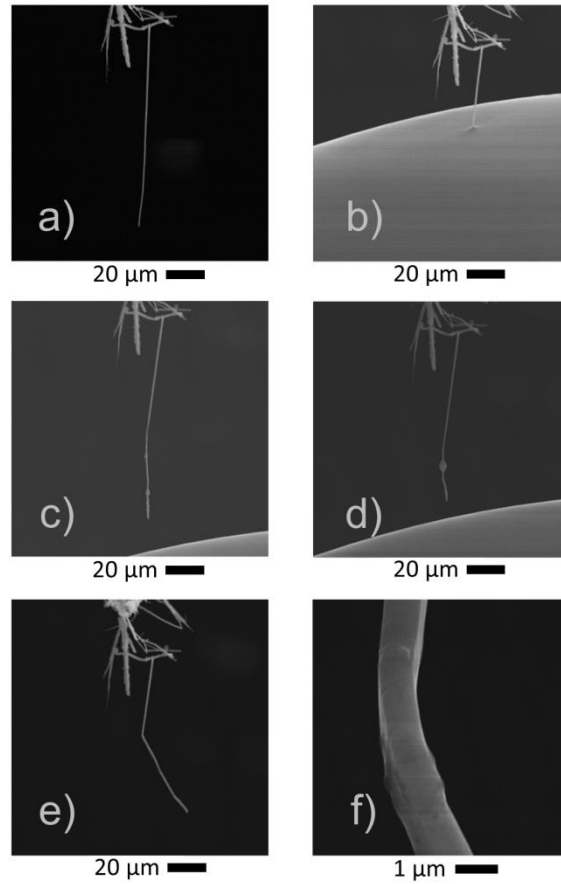


**Figure S1.** *In situ* morphological changes - bending: a) Initial shape of a V<sub>2</sub>O<sub>5</sub> whisker; b) Whisker submerged into electrolyte; c) Whisker pulled out of electrolyte after 2 charge-discharge cycles; d) after 3 cycles; e) final whisker distortion after 5 cycles; f) zoomed-in image of the formed kink in e).